THE TRACE TELESCOPE POINT SPREAD FUNCTION FOR THE 171 Å FILTER

S. Gburek[1], J. Sylwester[1] and P. Martens[2]

[1]*Space Research Centre, Polish Academy of Sciences, Solar Physics Division, Kopernika 11, 51-622 Wroclaw, Poland (`sg@cbk.pan.wroc.pl`)*
[2]*Montana State University, PO Box 173840, Bozeman, MT 59717*

Abstract. We perform an analysis of the TRACE telescope blur from EUV images. The blur pattern is discussed in terms of the telescope point spread function (PSF) for the 171 Å filter. The analysis performed consists of two steps. First, an initial shape for the PSF core is determined directly from TRACE EUV images. Second, the blind deconvolution method is used for obtaining the final PSF shape. The PSF core peak is fitted by analytical functions to determine its parametric characteristics. The determined PSF includes the core central peak and peaks caused by diffraction effects inherent in TRACE EUV data. The diffraction portion of the PSF is studied theoretically in the Fraunhofer diffraction limit. The temperature dependence of the TRACE PSF shape is investigated for a selected temperature range. We also discuss general properties of the obtained PSF and its possible applications.

Keywords: TRACE, PSF, Blind Deconvolution

1. Introduction

The Transition Region and Coronal Explorer (TRACE) satellite was launched from Vandenberg Air Force Base in USA on 2 April 1998 to perform observations of the solar photosphere, transition region, and corona with high spatial resolution and temporal continuity. The satellite itself is a NASA Small Explorer (SMEX) spacecraft. The TRACE Sun-synchronous polar orbit enables uninterrupted solar phenomena observations except during a few-month-long eclipse season when short interruptions occur. The TRACE satellite carries a 30 cm Cassegrain type telescope with a field of view of 8.5×8.5 arcmin and a spatial resolution of ~ 1 arcsec. The multilayer optics focus solar radiation on a CCD sensor of 1024×1024 pixels (1 pixel = 0.5 arcsec).

The incident photon signal is converted into a charge within each CCD pixel and then represented by the instrument electronics as so-called data number (DN). The signal value measured in DNs is kept within the range 0 - 4095 DN with a saturation level of 4095 DN. TRACE observes solar plasma in a selected temperature range from ~ 6000 K for white-light images up to ~ 20 MK for EUV ones with typical temporal resolution of less than one minute. More details about
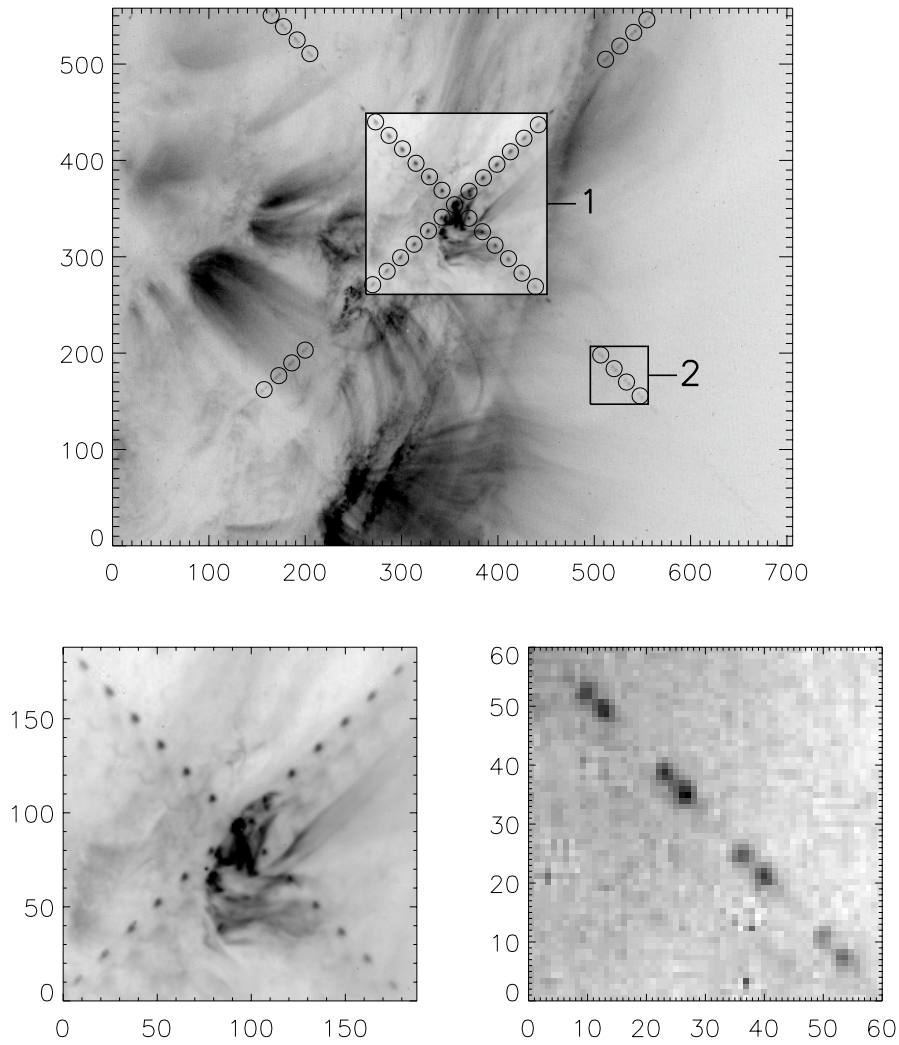
Figure 1. Top - TRACE 171 Å compact flare image taken on May 16, 1999 at 13:49:22 UT with an exposure time of 19.5 seconds. The TRACE PSF maxima are clearly visible extending outwards in four arms from the saturated flaring area. Encircled are the stronger maxima of orders $1-6$ and $11-14$ which are investigated in more detail in the present study. For presentation purposes different signal scaling was used for the image portion in box 1 containing maxima up to sixth order. This portion is shown enlarged in the bottom-left panel. The sub-image in box 2 with further diffraction structures of orders $11-14$ is expanded in the bottom-right panel.

the instrument can be found in Handy *et al.* (1999). A review of TRACE early observations is given by Schrijver *et al.* (1999).

As any optical system, the TRACE telescope introduces a certain amount of blur into its images. This blurring pattern can be discussed in terms of the telescope point spread function (PSF) which describes the response of the entire optics to a distant point source. Unlike for many other recently-flown high-energy imaging systems, the TRACE PSF is not a single peaked function. In addition to the main central peak - the core caused by geometrical imperfectness of the optics - the TRACE PSF contains other peaks which are formed as replications of the core due to diffraction by the nickel wire mesh supporting the telescope entrance filters.

2. TRACE PSF and diffraction pattern

The overall diffraction effects are particularly well observed in TRACE images of strong compact sources, such as the flaring kernels shown in Figure 1 and the top-left panels of Figures 2 and 3. The diffraction structures are spaced roughly every 20 pixels and arranged along two lines intersecting almost at right angles.

The shape of the diffraction structure changes apparently with order. They are of the form of sharp well-defined peaks only for the lowest six orders. For higher orders they become elongated and eventually split into double or multi-peaked structures. The overall signal intensity in the diffraction structures varies significantly with order. They fade out gradually and become invisible for the ninth order. For higher orders they brighten back and disappear again for order eighteen. In the images of stronger compact sources (Figure 1) the zeroth-order structure and the lower-order structures are often corrupted by saturation effects. The zeroth-order structure and the structures up to sixth order are however very visible in non-saturated TRACE images of relatively weak sources (see the top-left panels of Figure 2 and 3). From the inspection of data shown in the top-left panels of Figures 2 and 3, it is seen that in non-saturated TRACE images of compact sources the diffraction extends up to the sixth order. The diffraction structures in such images have the form of sharp peaks. In saturated TRACE frames, the diffraction is also seen in orders higher than the sixth (see Figure 1). In higher orders, the diffraction structures become non-uniformly shaped even if the observed source is compact. The shape changes of high-order diffraction structures occur due to large dispersion effects and the plasma conditions of the source upon which the incident spectrum is dependent.
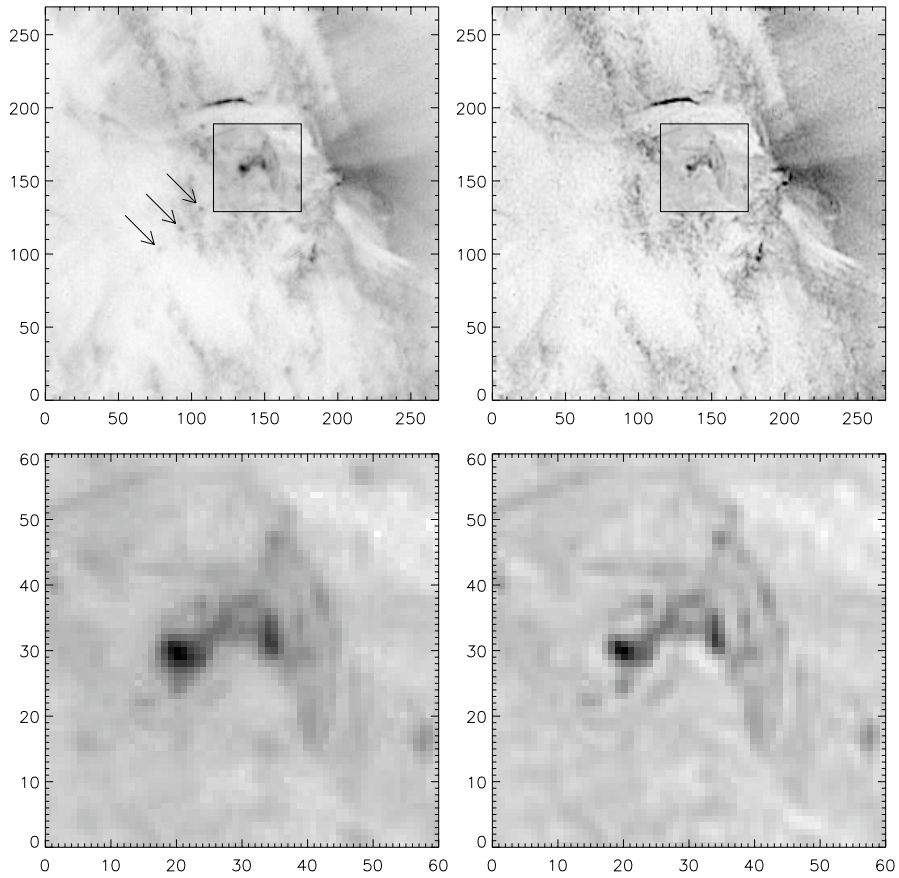
Figure 2. Top-left panel - a non-saturated image of a compact EUV flaring event observed by TRACE in the 171 Å filter on 21 October 1999 at 19:54:43 UT with an exposure time of five seconds. The diffraction effects are visible up to sixth order in this image (three of the diffraction structures seen in the lower-left pattern arm are indicated by arrows in the image). Top-right - deconvolved TRACE image corresponding to the image from the top-left panel. The central image portions (in the boxes) of both data and deconvolved frames are shown enlarged in the bottom-left and bottom-right panel, respectively.

The quantitative properties of the diffraction pattern seen in Figure 1 were determined by Lin, Nightingale, and Tarbell (2001). We performed a similar analysis taking into account the brightest structures not corrupted by saturation seen in diffraction orders $1-6$ and $11-14$. The analysis was performed for all four arms extending from the midpoint of the whole diffraction pattern in Figure 1. For each analyzed structure we determined its support (the image area in which the

structure signal exceeded three times the local noise level), subtracted background, and calculated its position and intensity in the pattern coordinate system. We defined the structure position as an average position in its support weighted by signal value. Thus, the position (x_c, y_c) of each particular structure in the image in Figure 1 is given by:

$$(x_c, y_c) = \frac{1}{n} \sum (i, j) I(i, j), \tag{1}$$

in which pairs (i, j) label the image pixel coordinates, $I(i, j)$ is the signal value in DN in pixel (i, j), n is a number of pixels in the neighborhood of the structure considered, and the summation runs only over the particular neighborhood. Such defined positions agree exactly with peak positions for structures of orders $1-6$. For the double-peaked structures of higher orders $(11-14)$ the positions are placed somewhere near the midpoint between the peaks. The intensity of each structure was calculated as an integral of the background-subtracted signal over the structure neighborhood.

We fitted two straight lines using linear regression to measure the geometry of the diffraction cross seen in Figure 1. The first line was fitted to the determined structure positions from the lower-left and the upper-right arms of the pattern. The second line was fitted to the structure positions from the lower-right and the upper-left arms. In both cases a very good quality fit was obtained with a correlation coefficient of 0.99. From the fit parameters we calculated the angle between fitted straight lines and the horizontal bottom image edge. These angles are $\phi_1 = 44.02°$ and $\phi_2 = 134.01°$ (counterclockwise) for the first and the second fitted lines respectively, so indeed the fitted lines are almost exactly orthogonal but do not run parallel to the CCD pixel diagonals (as it would be for $\phi_1 = 45°$ and $\phi_2 = 135°$).

It has been established by Lin, Nightingale, and Tarbell (2001), and independently here, that the structure intensity dependence on diffraction order can be well explained theoretically assuming the Fraunhofer diffraction limit for the TRACE telescope. In this approach, the structures seen in Figure 1 arise as principal maxima of the diffraction pattern produced by the two-dimensional grating with square openings (Lin, Nightingale, and Tarbell, 2001). The theory also says that the principal maxima intensities can be related to the zeroth-order peak intensity (I_0) by the following expression:

$$I_m = I_0 \left(\frac{sin(m\pi\beta)}{m\pi\beta} \right)^2, \tag{2}$$

in which $m = 0, 1, 2, ...$ is the diffraction order, I_m is the intensity of the m-th order maximum, β is a constant characteristic of the wire mesh
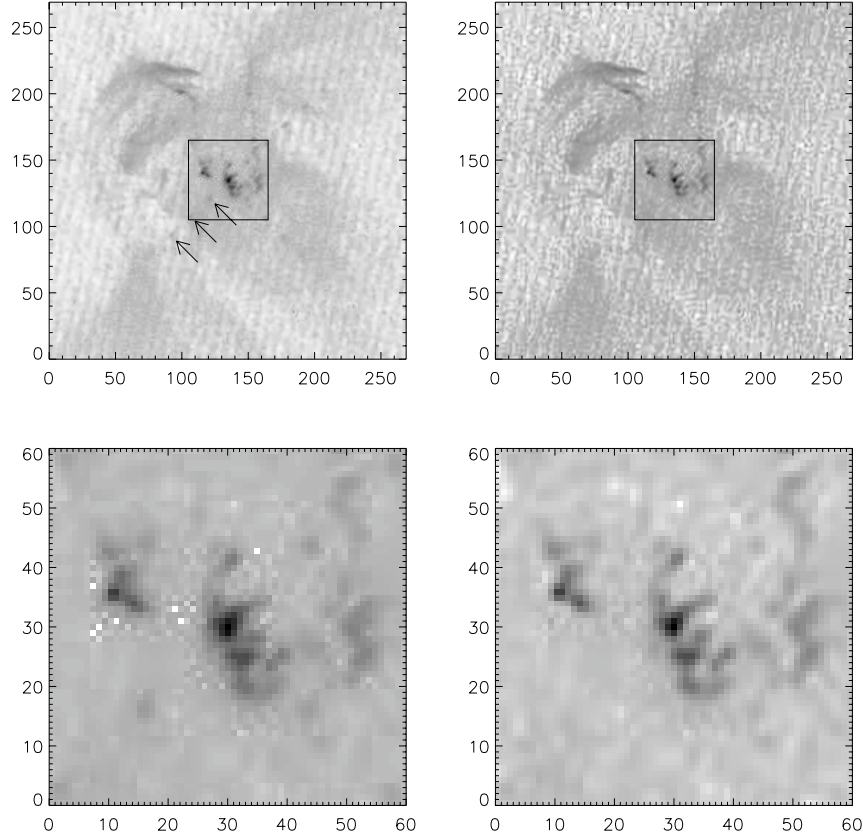
Figure 3. Top-left panel - a TRACE 171 Å compact flare image taken on June 19, 2001 at 09:56:46 UT with an exposure time of one second. The diffraction effects are visible up to sixth order in this image (three of the diffraction structures seen in the lower-left pattern arm are pointed to by arrows in the image). This image after deconvolution is shown in the top-right panel. The central portions of both data and deconvolved image (in the boxes) are enlarged in the bottom-left and bottom right panel, respectively.

geometry. Lin, Nightingale, and Tarbell (2001) calculated that for the TRACE entrance filter the mesh constant β equals 0.885.

Using the Fraunhofer theory of diffraction one can also derive an expression for the distance r_m of any principal maximum from the diffraction pattern center as a function of wavelength λ (Lin, Nightingale, and Tarbell, 2001). This expression reads:

$$r_m = m \frac{\lambda}{a},\tag{3}$$
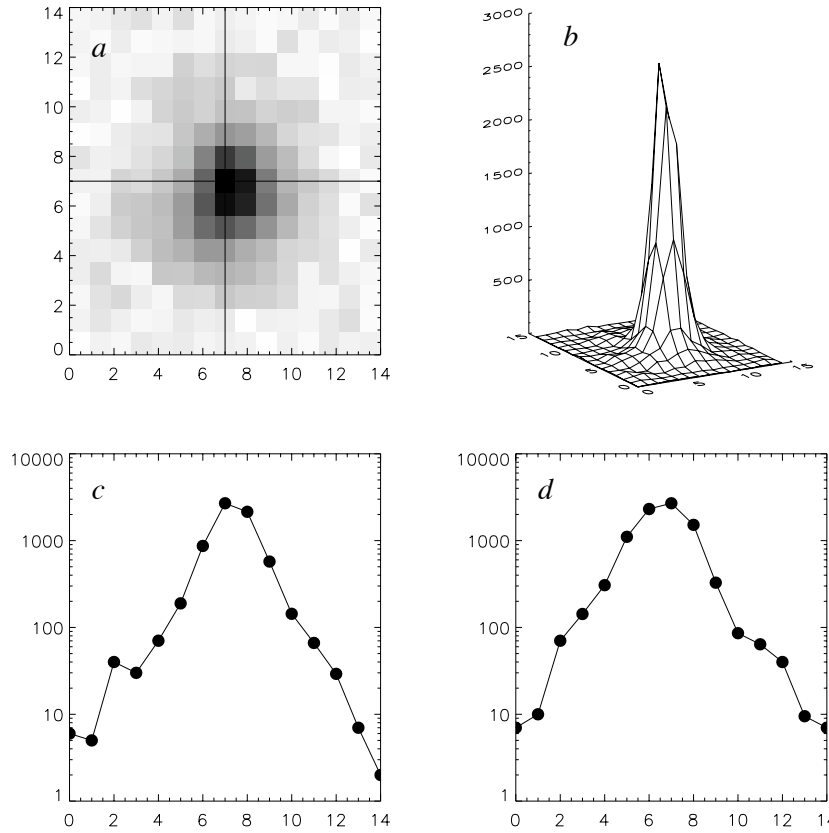
Figure 4. *a*: The enlarged image of the background-subtracted first-order maximum from the upper-left diffraction arm in Figure 1. *b*: a surface plot of the data from (*a*). *c* and *d*: the cross sections of the maximum along the horizontal and vertical lines shown in (*a*).

where m is the diffraction order, λ is the wavelength of incident radiation, and a is the distance between wires of the mesh. For the TRACE telescope $a = 3.63 \times 10^{-4}$ m (Handy *et al.*, 1999). For r_m in TRACE pixels and λ in Å, Equation (2) takes the form:

$$r_m = 0.113804\, m\, \lambda. \qquad (4)$$

The above discussed properties of the TRACE diffraction pattern allow modeling the PSF provided that the spectrum of incoming radiation and PSF core are known. Modeling of the PSF for a given shape of the illuminating spectrum consists of several steps. First, the solar spectrum has to be multiplied by the TRACE spectral response in order

to take into account the overall attenuation introduced by the instrument. The next step is to redistribute spectral intensities over the CCD starting from a certain point chosen as the diffraction pattern center (the position of the zeroth-order maximum). For proper redistribution, one needs to determine diffraction maxima positions in the pattern by using Equation (4) and angles ϕ_1, ϕ_2. Scaling of the subordinate peak intensities is then obtained from Equation (2). The redistribution procedure has to be repeated separately for each wavelength in the spectrum and the results summed together. Finally, the reconstructed diffraction pattern has to be convolved with the PSF core to account for instrument spatial blur and renormalized to unit integral. In principle, it is possible to reconstruct the TRACE PSF up to arbitrary diffraction order in this way. In practice, the PSF model is bounded by the CCD edges.

3. The core part of the TRACE PSF

Analysis of the TRACE telescope data, as well as measuring telescope instrumental blur and diffraction effects, requires the PSF core to be well determined. From the general method for reconstruction of the entire TRACE PSF from a given EUV spectrum, described in the previous section, it follows that the core PSF peak constitutes one of the essential components in the reconstruction process. Hence, in this section, we discuss the PSF core properties, determine its shape, and give its basic parametric characterization. In previous publications concerning the subject, it was determined from analysis of the cross-sections of the thinnest loops observed in TRACE data (Watko and Klimchuk, 2000)
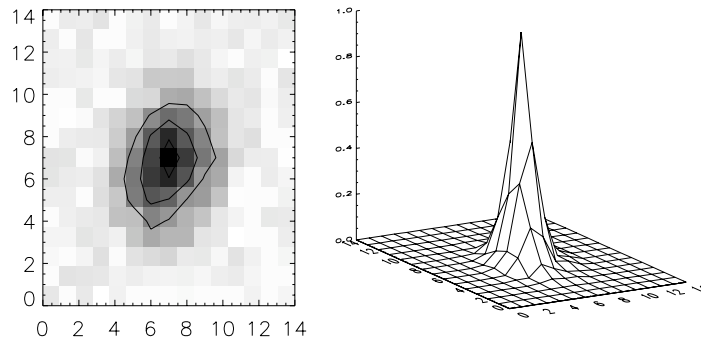
Figure 5. TRACE PSF core obtained by the SDM method.

that the TRACE PSF core full-width-at-half-maximum (FWHM) is about 2.5 pixels. The shape of the PSF core was also determined for the TRACE 171 Å channel using the blind iterative deconvolution (BID) method (Golub *et al.*, 1999). The shape obtained for this deconvolved core was asymmetric, being elongated approximately at the position angle of 45 degrees. The upper limit of the core FWHM was found to vary within the range from about two to about three pixels with position angle. The azimuthal average of the core FWHM over position angle was 2.5 pixels.

Here, in order to obtain a first raw approximation of the PSF core, we used the Steepest Descent Method (SDM) described in Gburek (2003). The final PSF core estimate was then obtained by blind deconvolution of the TRACE image. The SDM method has been applied earlier for determination of the PSF core of the SXT telescope. This method takes for input a sequence of non-saturated images of compact, narrow sources. Each image must be of the same fixed size and must have well-defined signal maxima in the center pixel. The images in the input sequence are then normalized to the range $[0, 1]$. Next, the normalized sequence is searched for the lowest signal at any pixel position. The minimum values for each pixel are collected in a new array of the size of the sequence images. The new array gives the approximation of the PSF core. It has been found that good initial estimates of PSF cores can be obtained by the SDM method provided that a good-quality image sequence had been chosen for the input. In particular, it has been noted that the more compact sources are present in images from the input sequence the more accurate are the PSF approximations obtained by the SDM method. Hence, we focused attention on the low-order (up to the sixth order) diffraction peaks seen in Figure 1. All of these peaks are quite narrow, especially the peaks of first and second order for which dispersion peak broadening is expected to be small. An example of a first-order peak and its cross-sections is shown in Figure 4. To prepare the initial image sequence for the SDM method, we took 15×15 pixel arrays centered at the peaks of low-order (up to sixth order), non-saturated, background-subtracted, diffraction maxima seen in Figure 1. The diffraction peak sequence was next processed with the above-described SDM method. The obtained approximation of the PSF core is shown in Figure 5. Its shape is a bit elongated roughly in the direction of the diagonal running from the lower-left to the upper-right corner of the image in Figure 5. The FWHM of the SDM-determined core approximation as estimated by fitting 2D Gaussian profile has been found to be 2.5 pixels.

The SDM-determined approximation of the PSF core was next used as the initial guess for blind deconvolution of TRACE images. It was

performed here using the modified iterative algorithm described by
Ayers and Dainty (1988). The algorithm is based on a telescopic image
formation model in which the observed count number in the data is
a pure convolution of the true brightness distribution of the imaged
object with the PSF. The algorithm is particularly applicable to images
with a high signal-to-noise ratio in which the noise contribution can be
assumed to be insignificant. The BID method starts from an initial
approximation for the PSF and performs iterative restoration of the
true brightness distribution by improving the PSF and cleaning the
image. The process of commutative restorations of the PSF and true
brightness distribution is repeated until a convergence limit threshold
is reached. As the algorithm convergence control criterion, a value of χ^2_ν
($\chi^2_\nu = \chi^2/(\nu - 1)$, where ν is the number of degrees of freedom) char-
acterizing the difference between data and reconvolved image and PSF
estimates at each iteration was calculated. The blind deconvolution
iterations were stopped when the minimum of χ^2_ν was found. Due to
noise in the data and the relative freedom in selection of the initial guess
for the PSF (which, in general, is different from the real PSF) expected
properties, such as non-negativity or conservation of the integral value
of the flux, are generally not preserved during the BID processing.
Hence, additional constraints were imposed on the recovered PSF and
image estimates in order to conserve the characteristics known to be
invariant at each iteration. Therefore, both estimates were forced to be
positive, the PSF estimate was renormalized to unit integral and the
integral flux of the restored image was kept constant at each iteration.

The positivity of the image and PSF estimates were imposed using
the same methods as described in detail by Ayers and Dainty (1988).
During each iteration, the renormalization of the PSF estimate took
place in the small areas surrounding PSF peaks. We estimated that
these areas contained more than 99 % of the entire PSF signal. Renor-
malization of the image estimate was performed in the areas where the
data signal was greater than the noise level. Tests on the synthetic data
showed that more than 98 % of the flux in the image can be restored
using this method.

The tests performed using synthetic data revealed that the BID
algorithm is capable of giving good restorations for both the image
and the PSF. Trial deconvolutions on real and test data showed also
that the performance and speed of the BID algorithm depend on the
initial guess for the shape of the PSF. After compatibility tests, the
deconvolution code will be integrated with the SolarSoft[1] environment.

---

[1] `http://www.lmsal.com/solarsoft/`

As we deconvolved the non-saturated TRACE data shown in the top-left panels of Figures 2 and 3, we prepared the initial PSF guess consisting of maxima up to sixth diffraction order. For the zeroth-order maximum we took the core approximation obtained by the SDM method. For preparation of the initial guess for the remaining maxima, one can use two methods. First, having the core approximation determined and the plasma parameters such as temperature and emission measure distribution known, at least for the brightest parts of the data to be deconvolved, one can generate the EUV spectrum of the observed solar radiation. Then the initial guess for the shape of higher order maxima can be modeled in the way described at the end of the previous section. On the other hand, for images of sources with well-localized emission, like the one in the top-left panels of Figures 2 and 3, one can determine the initial shape of higher order diffraction peaks directly from the image. We decided to go for the second approach and prepared the initial approximation of diffraction maxima of order $1-6$ from the background-subtracted diffraction peaks shown in Figure 1 and the top-left panels of Figures 2 and 3. The theoretical modeling of the TRACE PSF diffraction maxima in the isothermal approximation is discussed in the next section. The results of blind deconvolution are shown in Figure 6 and Figures 2 and 3.

In the deconvolved TRACE image there was a substantial increase in the signal range. The structures in the "clean" image were much sharper. The diffraction pattern was largely removed by deconvolution. No significant deformations of the image and PSF, which may come from noise or method artifacts, were detected. The value of χ^2_ν at the last iteration of deconvolution process was 0.90 and 0.51 for the deconvolution of data shown in Figures 2 and 3, respectively. We fitted elliptical Gaussian, Moffat, and Voigt functions to the deconvolved PSF core in order to give it a parametric characterization. We used Fourier-fitting methods which were previously applied for the PSF of the SXT telescope (Martens, Acton, and Lemen, 1995). This approach was found to be particularly useful for fitting spiky shapes such as the TRACE PSF core. We obtained the best quality fit with the Moffat function. Voigt fits were also of good quality in the peak but too fuzzy in the off-peak core areas. The worst fit was obtained using the Gaussian function. The comparison of various fitting results is shown in Figure 7.

Since the quality of the Moffat fit was the best, we decided to use this function to obtain a parametric characteristic of the TRACE PSF core.
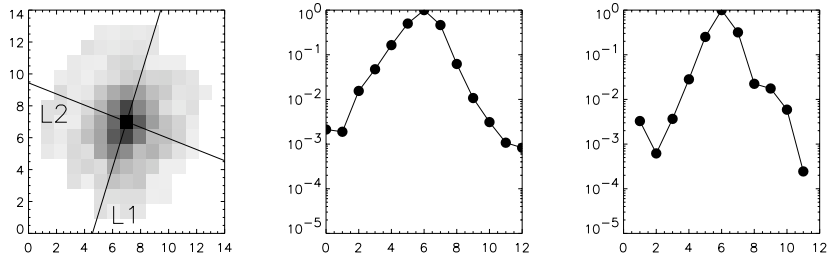
Figure 6. Left panel: deconvolved TRACE PSF core. Middle and right panels: the PSF core cross-sections along lines L1 and L2.

The mathematical expression for the Moffat function that we used is:

$$f(r) = c \left(1 + \frac{r^2}{a^2} \right)^{-b}, \tag{5}$$

in which r is the radial distance form the function peak ($r = \sqrt{x^2 + y^2}$ for planar Cartesian coordinates x, y) and a, b, c are parameters. This function defines a cylindrically symmetric surface in three-dimensional space with maximum value c and shape dependent on parameters a and b. To account for the observed elliptical deformations of the core, the r variable in Equation (5) has been redefined as follows:

$$r^2 = x^2(1 + \sqrt{\varepsilon_x^2 + \varepsilon_y^2} - \varepsilon_x) + y^2(1 + \sqrt{\varepsilon_x^2 + \varepsilon_y^2} + \varepsilon_x) - 2\varepsilon_y xy. \tag{6}$$

Such a modification gives an elliptically deformed Moffat function with ellipticity determined by parameters ε_x and ε_y. The two other parameters x_c and y_c were used for describing the offset of the fitting function peak position from the CCD pixel center. Hence, x and y in Equation (6) were redefined in the following way:

$$x = x - x_c, \quad y = y - y_c. \tag{7}$$

An additional, parameter bg was introduced to represent the background level. Hence, the form of the Moffat fitting function was fully described by eight parameters $(a, b, c, \varepsilon_x, \varepsilon_y, x_c, y_c, bg)$ exactly as was done for the SXT PSF in Martens, Acton, and Lemen (1995). The values of these parameters for the best fit are given in Table I. For Gaussian and Voigt fits we also allowed for elliptical deformations and off-center peak shift in the same way as described above for the Moffat function.

Table I. Parameters of the best elliptical Moffat fit to the TRACE PSF core.

a	b	c	x_c	y_c	ε_x	ε_y	bg
1.7405	2.3652	0.2114	-0.0518	-0.1100	-0.4520	0.3773	2.14×10^{-5}

From the parameter values collected in Table I, one can derive the essential characteristics of the PSF core: $FWHM = 2\,a\,\sqrt{2^{1/b} - 1} = 2.03$ pixels, and the angle of the longer axis of the elliptical PSF core deformation $\theta = (1/2)\arctan(\varepsilon_y/\varepsilon_x) = 70$ degrees counterclockwise to the horizontal edge of the TRACE images. The PSF core FWHM determined from the Moffat fit is significantly smaller than the one derived from the Gaussian fit. Our Gaussian core approximation gave a FWHM of 2.27 pixels – a result fairly consistent with the above-mentioned findings (Golub *et al.*, 1999), where also a Gaussian characterization of the PSF core was used.

Having the PSF core well characterized and with all of the necessary information about the TRACE diffraction pattern, one can reconstruct the entire TRACE PSF from solar spectra (see Section 2) and investigate the dependence of PSF geometry on the incident-spectrum properties. It is clear that for significantly different spectra, the shape of the PSF diffraction maxima must be substantially different in particular for higher diffraction orders.

One of the major factors that determines spectral intensities of a radiating plasma is its temperature either in continuum or lines. Especially line emission intensities are very sensitive to temperature changes. Hence, PSF diffraction maxima shape should vary significantly with temperature. Therefore, in the next section we study the temperature dependence of PSF shape for a selected temperature range. Possible applications of the PSF properties for determining plasma temperature are discussed as well.

4. Temperature dependence of the TRACE PSF

We used the method for TRACE PSF reconstruction described in Section 2 to determine the PSF for solar sources in the isothermal approximation.

For a better overview of the entire TRACE PSF pattern, we made a number of simulations assuming that the source plasma is isothermal and in the range of $0.5 - 20.0$ MK.
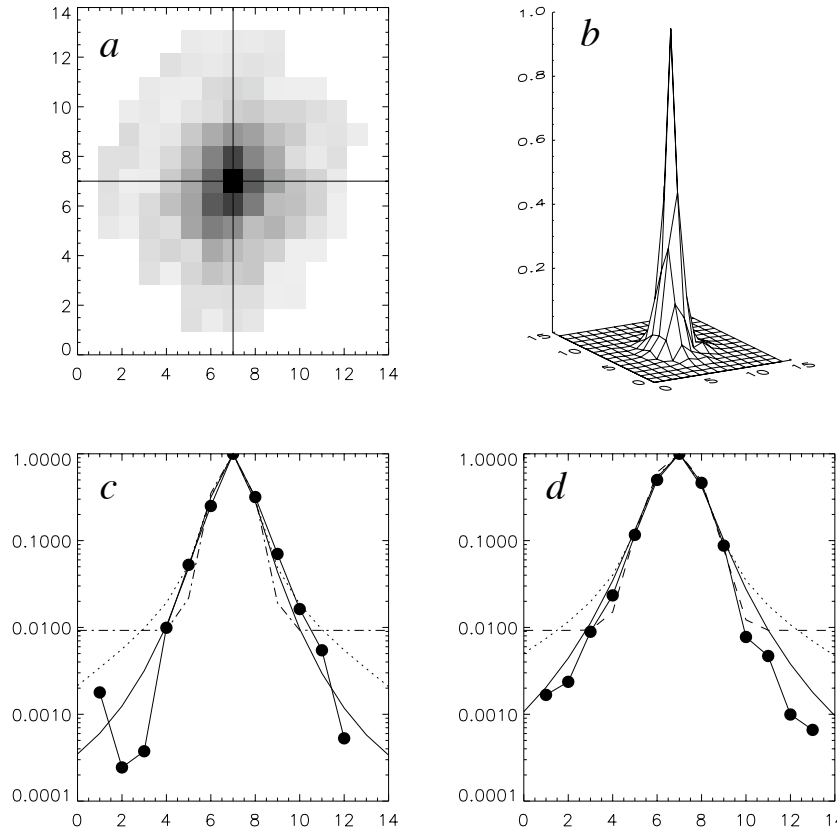
Figure 7. Image of the deconvolved TRACE PSF core (*a*) and its surface plot (*b*). In (*c*) and (*d*) the cross-sections of the peak along the horizontal and vertical lines in (*a*) are plotted. The PSF core cross-sections are plotted as a thick solid line with black dots. The corresponding cross-sections of the best fits to the core in terms of analytical functions are overplotted in (*c*) and (*d*). The Moffat function fit cross-sections are plotted in a thin solid line, for the Gaussian fit a dash-dotted line is used, and for the fit of the Voigt profile - the dotted line.

In order to determine the isothermal solar spectra illuminating the instrument, a synthetic spectrum was calculated using the CHIANTI atomic physics database[2]. CHIANTI is a freely-available, peer-reviewed, atomic physics database and software suite that allows a user to model spectral line and continuum emission from 1 Å to 600,000 Å using factors such as temperature, ionization equilibrium, and elemental abundances of the plasma as input parameters (Dere *et al.*, 2001; Young

---

[2] http://www.damtp.cam.ac.uk/user/astro/chianti/

et al., 2003). For our initial CHIANTI synthetic spectrum we used the ionization equilibrium calculations of Mazzotta *et al.* (1998) and the solar coronal abundances of Feldman (Feldman *et al.*, 1992; Allen, 1973) as our input parameters.

In order to obtain the contribution of a given solar spectrum to the signal which is measured on the TRACE CCD, one needs to multiply the spectrum of the incoming radiation by the spectral response curve for the TRACE filter in which the image is recorded. The spectral
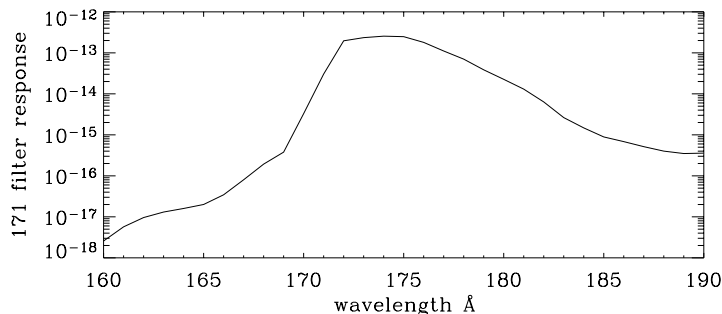
Figure 8. Spectral response curve for the TRACE 171 Å filter. The curve is given in units of $DN\,\mathrm{cm}^2\,\mathrm{sr}\,\mathrm{photon}^{-1}\,\mathrm{pixel}^{-1}$.

response curves define how the radiation intensity for any particular wavelength is attenuated by the overall instrument optics. For each of the TRACE filters the spectral response curves can be obtained using standard TRACE data analysis software. The plot of this curve for the TRACE 171 Å channel is shown in Figure 8. The multiplication by the spectral response curve of the 171 Å channel significantly changes the spectrum. The continuum shape and line intensities are modified according to the response curve. The intensities at the edges of the band are substantially attenuated. The counterparts of the isothermal spectra, multiplied by the spectral response function of the 171 Å filter (the so-called spectral signal contribution functions), are shown in Figure 9. The overall character of the spectra modified by the instrument spectral response function does not change substantially, in the sense that both lines and continuum give substantial contribution to the observed flux The intense line emission observed for the lower temperature regime disappears almost completely for the higher temperatures where the continuum emission, with only a few stronger lines, becomes the major factor contributing to the observed flux. For lower temperatures, 0.5 MK and 1.0 MK, the lines of Fe IX and Fe X ions dominate in the TRACE 171 Å channel. At about 3.0 MK the lines of Ni XV and Ca XV
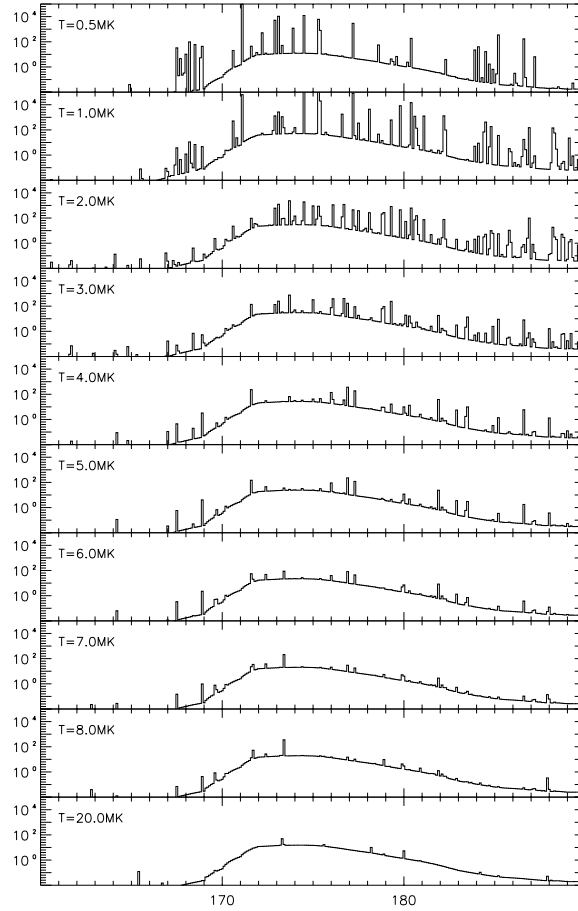
Figure 9. Isothermal spectral contribution functions to the TRACE image signal as calculated for a range of temperatures. The units on the y-axes of the plots are $DN\,\mathrm{s}^{-1}\,\mathrm{pixel}^{-1}$.

ions start to take over. For higher temperatures around $5-6$ MK the iron line emission is dominant again this time in lines of Fe XX , Fe XXI, Fe XXII and Fe XXIII ions.

In the next step of our analysis, we consider in more detail the dependence of the TRACE diffraction pattern on the temperature. We used spectra corrected for 171 Å filter response to construct the TRACE PSF shapes in the isothermal approximation. The spectral signal contribu-

tion functions shown in Figure 9 were accordingly redistributed over the
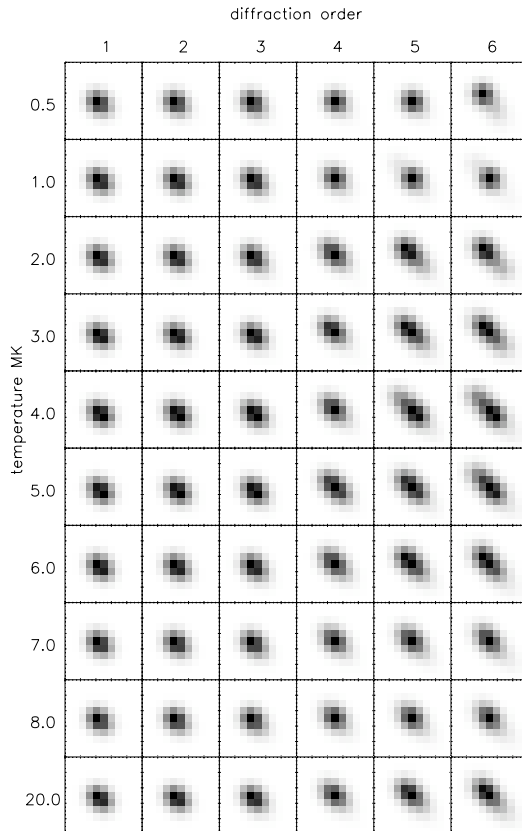
Figure 10. Temperature variability of the individual shape of the TRACE PSF diffraction structures (for orders 1 −6) obtained in the isothermal approximation. Each individual structure was constructed using CHIANTI isothermal spectra multiplied by the TRACE effective area function, and convolved with the PSF core determined from blind deconvolution. The size of each small panel in this figure is 11×11 TRACE pixels.

CCD starting from the CCD center using the dispersion Equation (4) and the diffraction pattern geometry defined by the angles ϕ_1, ϕ_2. Order-dependent intensity changes were calculated using Equation (2) for each wavelength separately and summed together. Next the resulting diffraction pattern was convolved with the PSF core determined from blind deconvolution to introduce telescope blur and the entire PSF was normalized to the unit integral.

By looking at the modeled PSF surface we observed that the individual PSF peak shape depends strongly on the temperature, especially for higher diffraction orders. The variation of the TRACE
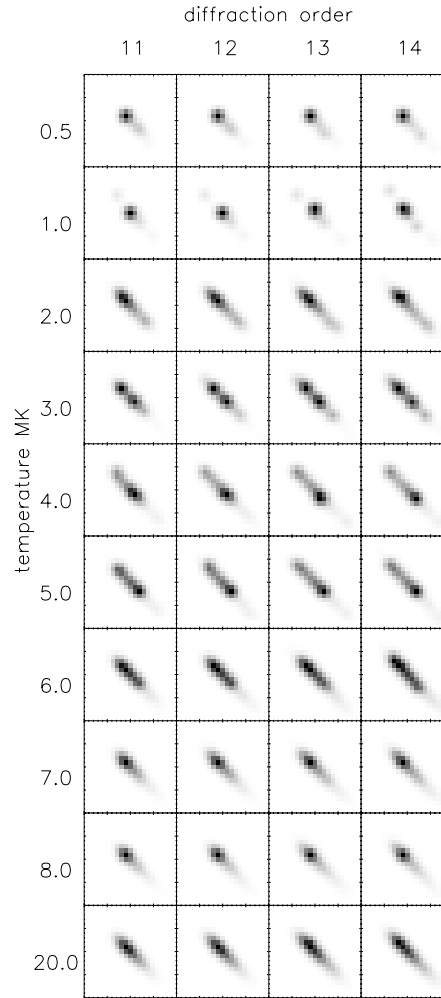
Figure 11. Temperature variability of the individual shape of the TRACE PSF diffraction structures (for orders 11 – 14) obtained in the isothermal approximation. Each individual structure was constructed using CHIANTI isothermal spectra multiplied by the TRACE effective area function, and convolved with the PSF core determined from blind deconvolution. The size of each small panel in this figure is 21 × 21 TRACE pixels.

PSF pattern with the source plasma temperature is shown in detail in Figures 10 and 11. Only the lower-order maxima (up to the sixth order) keep the form of more or less fuzzy, but well-defined, single compact peaks in the 0.5 – 20.0 MK temperature range analyzed. Over the entire range, the temperature variations of higher-order diffraction peaks become dramatic reflecting a strong dependence of the spectral

contribution functions on the source temperature. This dependence of the diffraction pattern on the temperature paves the way for potential use of this effect in detailed mapping of the temperature distribution for flaring kernels.

5. Conclusions

The PSF core for the TRACE telescope was deconvolved and fitted with Gaussian, Moffat, and Voigt functions. The best fit was obtained with the Moffat function. The Gaussian and Voigt fits gave less accurate characteristics of the core. Both of them are too fuzzy in the off-peak areas.

The deconvolved PSF core is a very sharply peaked and elliptically deformed function. From elliptical Moffat fits we found that the position angle of the longer ellipse axis is 70 degrees and that the core FWHM is 2.03 pixels.

Deconvolution of TRACE images substantially increases the image dynamic range and sharpens the structures seen. The diffraction portion of the PSF can be largely removed from images by deconvolution.

The PSF subordinate diffraction peak shapes and intensities are very sensitive to the temperature as is seen from isothermal modeling of the PSF diffraction pattern. This is a particularly important effect influencing the shape and internal structure of the diffraction peaks observed for orders greater than ten. Substantial temperature dependence of the PSF high-order diffraction emission suggests that even single TRACE images can be used for the analysis of the temperature and emission measure distribution in the source if the diffraction pattern is of significant magnitude in the image.

Acknowledgements

References

Allen, C.W.: 1973, *Astrophysical quantities,* University of London, Athlone Press, 3rd ed., London.

Ayers, J.R. and Dainty, J.C.: 1988, *Optic Letters* **13**(7), 547.

Dere, K.P., Landi, E., Mason, H.E., Monsignori-Fossi, B.C., and Young, P.R.: 1997, *Astron. Astrophys. Suppl. Ser.* **125**, 149.

Feldman, U., Mandelbaum, P., Seely, J.F., Doschek, G.A., and Gursky, H.: 1992, *Astrophys. J. Suppl.* **81**, 387.

Gburek, S.: 2003, *PhD thesis*, Space Research Centre, Polish Academy of Sciences.

Golub, L., Bookbinder, J., Deluca, E., Karovska, M., Warren, H., Schrijver, C.J. *et al.*: 1999, *Phys. Plasmas* **6**(no. 5), 2205.

Handy, B.N., Acton, L.W., Kankelborg, C.C., Wolfson, C.J., Akin, D.J., Bruner, M.E. *et al.*: 1999, *Solar Phys.* **187**, 229.

Lin, A.C., Nightingale, R.W., and Tarbell, T.D.: 2001, *Solar Phys.* **198**, 385.

Martens, P.C.H., Acton, L.W., and Lemen, J.R.: 1995, *Solar Phys.* **157**, 141.

Mazzotta, P., Mazzitelli, G., Colafrancesco, S., and Vittorio, N.: 1998, *Astrophys. J. Suppl.* **133**, 403.

Schrijver, C.J., Title, A.M., Berger, T.E., Fletcher, L., Hurlburt, N.E., Nightingale, R.W. *et al.*: 1999, *Solar Phys.* **187**, 261.

Watko, J.A. and Klimchuk, J.A.: 2000, *Solar Phys.* **193**, 77.

Young, P.R., Del Zanna, G., Landi, E., Dere, K.P., Mason, H.E., and Landini, M.: 2003, *Astrophys. J. Suppl.* **144**, 135.